

Tailoring the coordination microenvironment of single-atom W for efficient photocatalytic CO₂ reduction



Jinyu Zhou ^{a,f,1}, Xiuling Zha ^{a,b,1}, Zhigang Chen ^a, Kaining Li ^e, Hongzhao Sun ^{a,f}, Juan Wang ^{d,*}, Kangle Lv ^{e,*}, Shan Cong ^{a,b,c,***}, Zhigang Zhao ^{a,b}

^a Key Lab of Nanodevices and Applications, Suzhou Institute of Nano-Tech and Nano-Bionics, Chinese Academy of Sciences, Suzhou 215123, China

^b Nano Science and Technology Institute, University of Science and Technology of China (USTC), Suzhou 215123, China

^c Division of Nanomaterials and Jiangxi Key Lab of Carbone Materials, Jiangxi Institute of Nanotechnology Nanchang 330200, China

^d Shanghai Synchrotron Radiation Facility (SSRF), Shanghai Advanced Research Institute, Chinese Academy of Sciences, Shanghai 201204, China

^e Key Laboratory of Resources Conversion and Pollution Control of the State Ethnic Affairs Commission, College of Resources and Environment, South-Central Minzu University, Wuhan 430074, China

^f Jiangsu Key Laboratory of Micro and Nano Heat Fluid Flow Technology and Energy Application, School of Physical Science and Technology, Suzhou University of Science and Technology, Suzhou 215009, China

ARTICLE INFO

Keywords:
Modulable coordination
Single atom tungsten
Photocatalysis
Carbon dioxide reduction

ABSTRACT

Fine-tuning the coordination number of single-atom W has been achieved by anchoring single-atom incorporated onto Graphite carbon nitride ($\text{g-C}_3\text{N}_4$) frameworks, which has been found to be essential for efficient photocatalytic CO₂ reduction. The WN₄ sample, with a moderate coordination number of 4 for W atoms, exhibits the highest photocatalytic activity toward CO yield at $2.67 \mu\text{mol h}^{-1}\text{g}^{-1}$, several times larger than the W sites with other coordination numbers such as 3 and 5. The coordination microenvironment of central W sites is found to be crucial for CO₂ chemisorption and efficient charge-carrier separation/transport during photocatalytic reactions. These results suggest that the coordination microenvironment of single atoms plays a significant role in photocatalytic reactions, providing insights into the design of single atoms catalysts suitable for photocatalytic applications.

1. Introduction

Excessive carbon emissions, primarily in the form of gaseous carbon dioxide (CO₂) resulting from fuel combustion, have garnered global attention [1]. Various carbon-neutral strategies have recently been developed as artificial controls on the carbon cycling [2,3]. Photocatalytic reduction is considered a highly promising method for CO₂ remediation, as it directly converts CO₂ back into chemical fuels such as CO, CH₄, HCOOH with only the input of light and water [4,5]. However, due to the chemical inertness of CO₂, effectively capturing and activating this molecule on catalyst surfaces presents a significant challenge in the search for desirable photocatalysts. Tremendous progress has been made in developing photocatalysts with improved CO₂ reduction activities, including the recent emergence of single-atom catalysts

(SACs) that combine the advantages of both homogeneous and heterogeneous catalysts which have just been employed in photocatalytic reactions in the past few years [6–8].

SACs are characterized by isolated metal atoms anchored on heterogeneous supports, which can be regarded as homogeneous catalysts with the supports acting as rigid ligands in terms of coordination chemistry [9,10]. Therefore, SACs possess a customizable coordination microenvironment and tunable electronic structures, offering the possibilities for simultaneous achievement of efficient light absorption, fast charge transfer and reduced activation energy for surface reactions which are known as key contributors to optimize the photocatalytic CO₂ reduction reaction (CO₂RR). In contrast to the extensive studies of SACs for electrocatalytic reactions (such as OER and ORR) since their introduction as electrocatalysts in 2011 [11], results demonstrating the

* Corresponding authors.

** Corresponding author at: Key Lab of Nanodevices and Applications, Suzhou Institute of Nano-Tech and Nano-Bionics, Chinese Academy of Sciences, Suzhou 215123, China.

E-mail addresses: wangjuan@sari.ac.cn (J. Wang), lvkangle@mail.scuec.edu.cn (K. Lv), scong2012@sinano.ac.cn (S. Cong).

¹ These authors contribute equally to this work.

feasibility of SACs applied in photocatalytic reactions remain rare till today [12]. Regarding photocatalytic activities, the decisive role played by local coordination microenvironment of SACs has just been inferred by several pioneer investigations very recently. For instance, Dong et al. have suggested that Ni–N₂O₂ moiety is more active for photocatalytic CO₂RR with respect to the traditional Ni–N₄ coordination structure, achieving remarkable CO generation ability with a high selectivity of 96% over H₂ [13]. By constructing single-atom sites of W⁵⁺–O–Ti³⁺ with oxygen-coordination at the intrinsic steps of TiO₂ nanoparticles, Feng et al. have reported enhanced photocatalytic CO₂RR efficiency with selectivity for methane (CH₄) over carbon monoxide (CO) [14]. However, there are still gaps between current achievements and a clear understanding about the photocatalytic behaviors depended on local coordination of single atoms. Especially, a fine-tuning toward coordination microenvironment of SACs remains a great challenge, which is largely restricted by the limited coordination number of the commonly investigated metals as SACs.

Tungsten is a Group 6 transition metal in the Periodic Table of Elements, remarkable for its complex electronic structure featuring open d and f shells, which is able to form a number of oxidation states (e.g., from +4 to +6), thus providing a large variety in its coordination numbers. When applied with flexible supports such as graphitic carbon nitride (g-C₃N₄), abundant explicit N species and N-coordinating cavities provided by the conjugated porous carbon nitride frameworks may act as anchoring sites for W atoms with the formation of W–N species. The generated W–N species have long been suggested to have somewhat platinum-like behavior due to its modified d-band electron structure with a greater density of states (DOS) near the Fermi level, which would be further manipulated for the optimization of efficient light absorption, moderate chemisorption and fast charge transfer to facilitate the photocatalytic CO₂RR [15,16].

Herein, atomically dispersed W atoms are incorporated into g-C₃N₄ via a hydrothermal process, followed by fine tuning over the coordination of the W sites by means of a post annealing treatment under NH₃ atmosphere. It is found that the coordination microenvironment of the central W plays a vital role in determining activity of photocatalytic CO₂RR, which can be optimized when a moderate coordination number of 4 (WN₄) is achieved. The WN₄ exhibits the prominent CO yield of 2.67 $\mu\text{mol h}^{-1}\text{g}^{-1}$, several times larger than the W sites with other coordination numbers such as 3 and 5, which is then disclosed to be related with enhanced CO₂ chemisorption and efficient charge-carrier separation/transport realized by fine-tuning of the W–N coordination number. This is the first report, to the best of our knowledge, on coordination-number dependent photocatalytic CO₂RR activity by constructing W-based SACs with a systematically modulated microenvironment, which would shed light on the design of SACs with advanced photocatalytic

performances.

2. Results and discussion

2.1. Synthesis and characterizations

Graphite carbon nitride (g-C₃N₄) is a typical non-metal photocatalyst with economic cost, nontoxicity, visible-light response, high chemical stability and proper band structure for CO₂ reduction [17]. As a layered polymeric material, g-C₃N₄ has also been widely employed as versatile support to stabilize single metal atoms, benefiting from the abundant electron rich pyridinic nitrogen atoms at the sixfold cavity which can offer rich coordination sites for metal atom anchoring [18]. The preparation of single-atom W atom loaded on g-C₃N₄ with controllable coordination is achieved by a four-step synthesis followed by post annealing treatments, as schematically illustrated in Fig. 1. First, melamine is employed as single precursor for the generation of g-C₃N₄ by a thermal-induced polymerization reaction. Then, tungsten species are incorporated into the g-C₃N₄ framework through hydrothermal reactions at 180 °C, with Na₂WO₄ and hydrochloric acid as reactants. In the following step, the products are crystallized via molten-salt reactions, to form thermodynamically stable configurations between tungsten species and the g-C₃N₄ lattice. Thus, excessive tungsten-oxide species (as dehydrated products from the H₂WO₄ intermediate) can be removed through alkaline leaching with concentrated KOH (3 M), leaving the W atoms anchored onto g-C₃N₄ (denoted as WN_x). Finally, the coordination of the WN_x species is allowed to be manipulated under NH₃ atmosphere in the post annealing steps, which is treated at temperatures of 450 and 500 °C, respectively [19]. The detailed processes are presented in the Experimental Section (Supplementary Information).

The successful synthesis of target WN_x products are first verified by X-ray diffraction (XRD) measurements. The three WN_x samples, denoted as WN₃, WN₄ and WN₅, depict nearly identical XRD patterns to the pristine g-C₃N₄ support, as indicated by a sharp peak at 27 ° and a relatively weak peak at 14 ° attributable to the (002) and (100) lattice plane of layered g-C₃N₄ material, respectively (Figure S1) [20]. No other peaks such as those related to W-related species can be observed in the XRD patterns, verifying the phase-pure property of the as-prepared samples [21]. Raman spectroscopy confirms the similarity in phase compositions between WN_x samples and the pristine g-C₃N₄ support (Figure S2), which is clearly inferred by the vibrational bands at 705 cm^{-1} and 1234 cm^{-1} that can be well ascribed to the layer-layer deformation and =C (sp²) bending of g-C₃N₄, respectively [22]. Noting that relatively weak intensities in the two peaks are observed for the WN_x samples with respect to pristine g-C₃N₄, indicating a weakened layer-layer interaction in g-C₃N₄ possibly induced by the anchoring of W

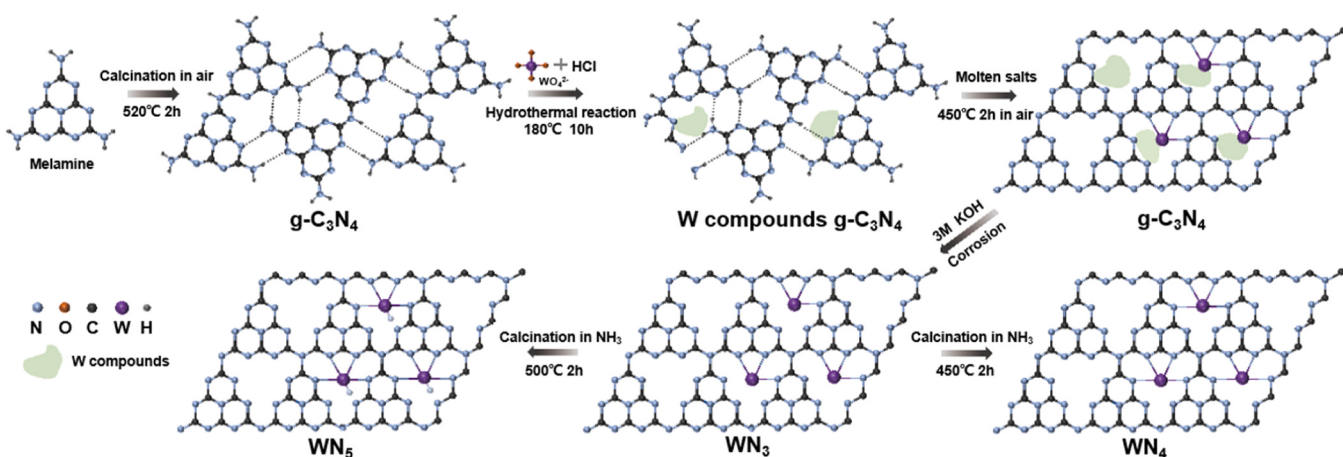


Fig. 1. Schematic illustration for the fabrication WN_x samples with modifiable W–N coordination (WN₃, WN₄ and WN₅).

species [23,24]

As the supporting framework, the g-C₃N₄ exhibits a typical layered morphology even unaffected by W incorporation and the post annealing processes, as depicted by the transmission electron microscopy (TEM) images (Fig. 2a and Figure S3). The atomically dispersed W species into the g-C₃N₄ lattice can be directly reflected by the high-angle annular dark field scanning transmission electron microscopy (HAADF-STEM), due to the large contrast between heavy metal atoms (W) and the lattice background constructed with light element of C and N. Similar images are depicted by the three WN_x samples, featured by a large number of bright spots well dispersed over the whole g-C₃N₄ framework (Fig. 2d-f). The intensity profile along the W atoms indicated by the yellow solid circle (inset in Fig. 2b) confirms that the isolated bright spot is of single-atom size (ca. 1.08 Å), which is further verified by the lateral dimensions of 200 bright spots measured in Fig. 2c. Elemental composition is then confirmed with the energy dispersive X-ray (EDS) elemental mapping, which reveals that C, N, O, and W are distributed homogeneously across the architecture (Figure S4). Notably, an approximate W loading amount can be revealed by the EDS results with the average ratio estimated to be ca 6.2 wt% for the three WN_x samples, meanwhile, the N/C ratio is kept almost the same between the WN_x and the pristine g-C₃N₄ samples (ranging from 1.65 to 1.69), suggesting the maintenance of the g-C₃N₄ lattice framework during the W-loading processing (Table S1). The existence of O element can be ascribed to the coordination between oxygen and W species that anchor on the g-C₃N₄ lattice.

2.2. Coordination environment of the single-atom tungsten

The g-C₃N₄ lattice plane has a unique pore structure composed of

three pyridine N atoms [23]. Such porous structure would provide anchoring sites for metal atoms through the strong bonding interaction between the *p*-orbitals of pyridine N atoms and the *d/p* orbitals of the metal atoms [22]. For a close investigation about the electronic structure and local coordination evolution from g-C₃N₄ to the three WN_x samples, high-resolution XPS and X-ray absorption fine structure (XAFS) analyses are performed. As shown in Fig. 3a, the W 4f XPS spectra of the three WN_x samples exhibit doublet peaks located at 35.02 and 37.14 eV attributable to W 4f_{5/2} and W 4f_{7/2}, respectively, implying that W atoms in our single-atom samples are predominantly in W-N bonding states [25]. To reveal the bonding between W atoms and the g-C₃N₄ supports, relevant auxiliary information can be obtained from the bonded non-metal atoms N1s XPS spectrum (Fig. 3b), which can be deconvoluted into three peaks, with the one at 398.7, 400.2 and 401.2 eV attributable to the double-coordinated N₂ (C=N=C), triple-coordinated N₃ (N-C)₃ and C-NH_x, respectively [26,27]. It is worthy of noting that the N₂:N₃ ratio decreases monotonously from 8.33 for pristine g-C₃N₄ to 5.55, 4.76 and 4.16 for WN₃, WN₄ and WN₅, respectively. Such a lowered N₂:N₃ ratio from g-C₃N₄ to WN_x samples indicates that W single atoms are preferably anchored by the double-coordinated N in g-C₃N₄, demonstrating the feasibility of further modulations in coordination numbers [28].

In order to quantitatively determine the specific W-N coordination number at monatomic tungsten sites, XAFS spectroscopy is employed for a refined structural resolution of W and N in the WN_x samples. As shown by the X-ray pre-edge absorption (XANES) and of the W L₃-edge (Fig. 3c), the near-edge shoulder for the three WN_x samples are located between those of W and WO₃, suggesting the existence of positively charged W species (typically between 0 and +6 valence) in the WN_x

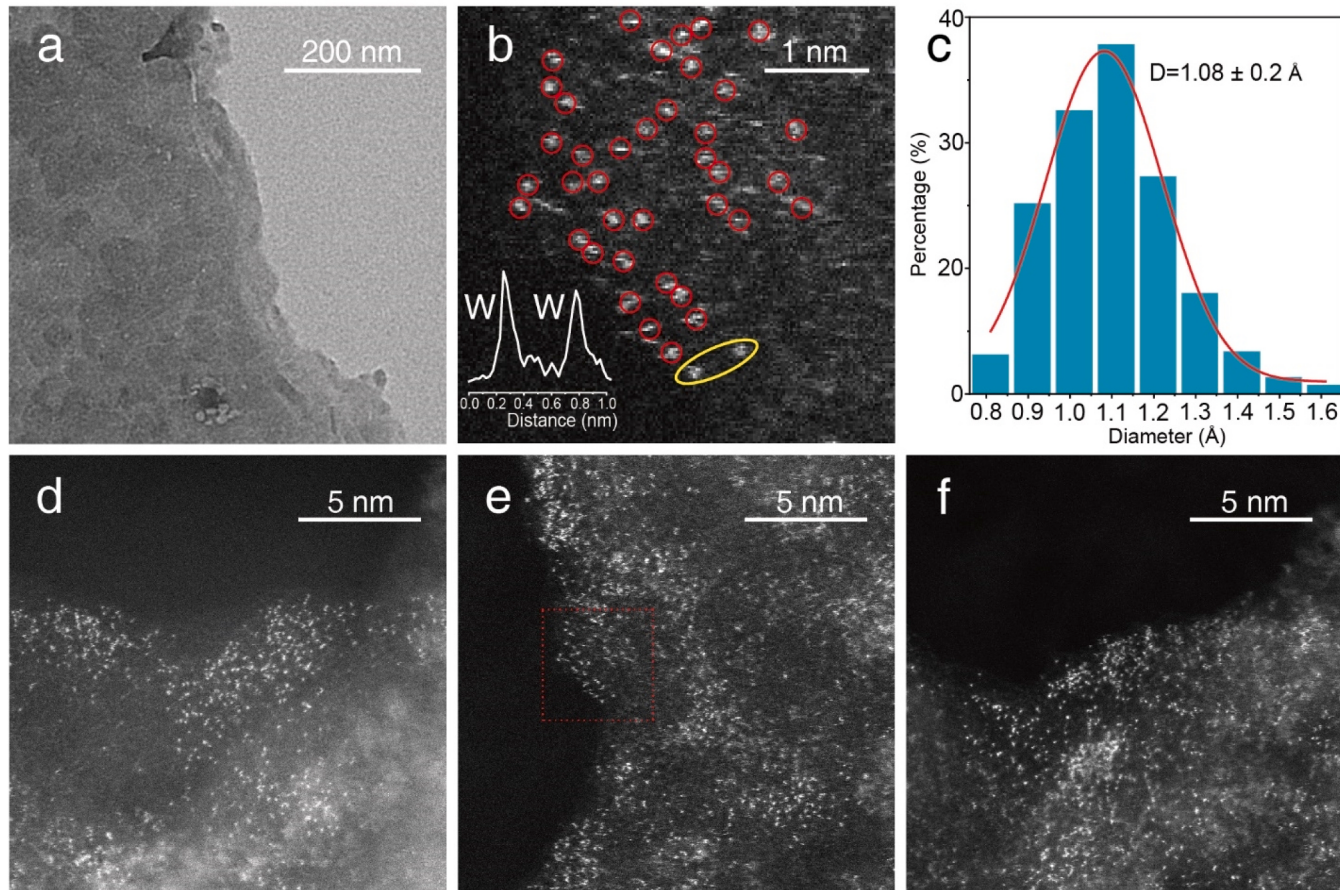


Fig. 2. (a) TEM image of WN₄. (b) Enlarged HAADF-STEM image of W single atoms in WN₄, inset shows the intensity profile along the W atoms indicated by the yellow solid circle. (c) Statistical analysis of the lateral dimension of atomically dispersed W atoms in (d). HAADF-STEM images of (d) WN₃, (e) WN₄, (f) WN₅ samples.

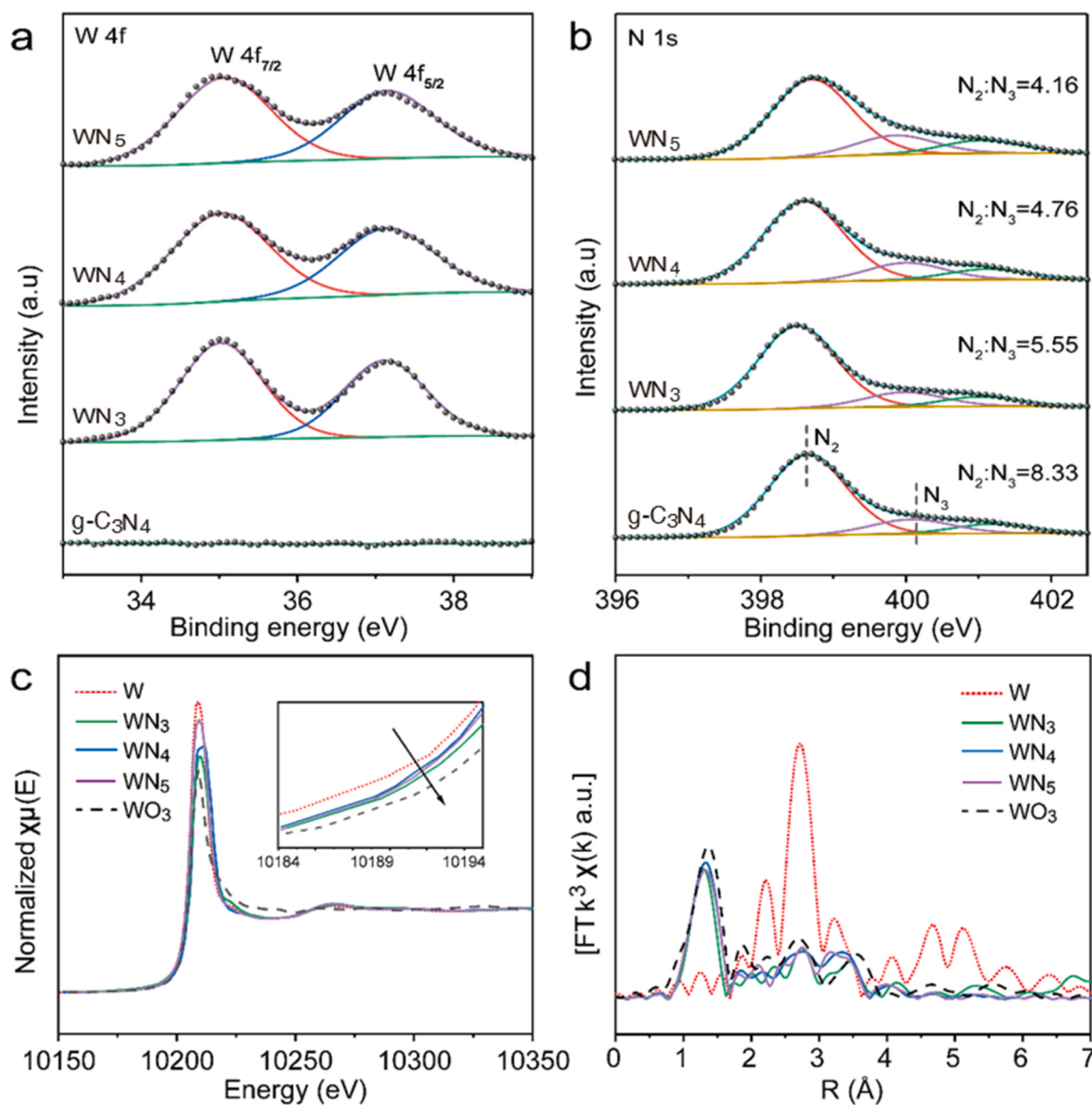


Fig. 3. (a) W 4f core level XPS spectra and (b) N 1s core level XPS spectra of the WN_3 , WN_4 , WN_5 and $\text{g-C}_3\text{N}_4$ samples. (c) XANES and (d) EXAFS spectra of WN_3 , WN_4 , WN_5 , and the reference samples of W foil and WO_3 powder. The inset is a magnified view of the pre-edge region in (c).

samples [29]. The Fourier-transformed extended X-ray absorption fine structure (EXAFS) spectrum of WN_x exhibit the dominant W-N peak centered at ca. 1.5 Å, instead no characteristic peak attributable to the W-W bond (located at ca. 2.8 Å as inferred by the reference tungsten foil) can be observed (Fig. 3d). The above results confirm the atomic W dispersion on the $\text{g-C}_3\text{N}_4$ framework and the absence of metallic W clusters in the WN_x samples, which are in consistent with the observations from TEM images. Further, quantitative structural parameters, including the coordination number and bond length of each WN_x sample, can be obtained by fitting the R-space of the EXAFS spectra (Figure S5). As extracted by the data in Table S2, the single-atom W in the WN_3 sample is coordinated with three in-plane N atoms, and two O atoms in z-axis approaching from the top and back directions of the plane, respectively. While altered coordination environment can be achieved in the WN_4 and WN_5 samples, which both contain four in-plane W-N bonds, leaving one z-axis coordination with O and N in WN_4 and WN_5 sample, respectively. Clearly, the chemical environment of central W sites in the WN_x samples can be delicately tailored by modifiable coordination numbers from 3 to 5, which would cause different photocatalytic activities toward CO_2RR .

2.3. Photocatalytic CO_2RR with WN_x samples

The photocatalytic activities of the WN_x samples regarding the coordination microenvironment at W sites are estimated by photocatalytic CO_2RR under visible light irradiation ($\lambda \geq 420$ nm) without the addition of any sacrificial agent. The main product of the photocatalytic CO_2RR is CO, while no other products from CO_2 reduction (such as CH_4 and HCOOH) can be detectable, suggesting a high selectivity when WN_x are employed as photocatalysts for CO_2RR . Fig. 4a compares the CO evolution amount versus irradiation time over different catalysts, while with the other experimental conditions keeping the same. The pristine $\text{g-C}_3\text{N}_4$ is inefficient for photocatalytic CO_2RR , with undetectable CO generation even lower than the limit of detection measured by an automatic online system for trace gas analysis. It is similar to previous observations, where the poor photocatalytic CO_2 reduction performances of $\text{g-C}_3\text{N}_4$ are mainly ascribed to inefficient charge transfer and poor CO_2 adsorption/activation capacity [30]. In contrast, continuous CO evolution (examined for over 4 h) as the product of CO_2RR can be observed with all the three WN_x samples under visible irradiation, clearly suggesting the contributions from single-atom W sites.

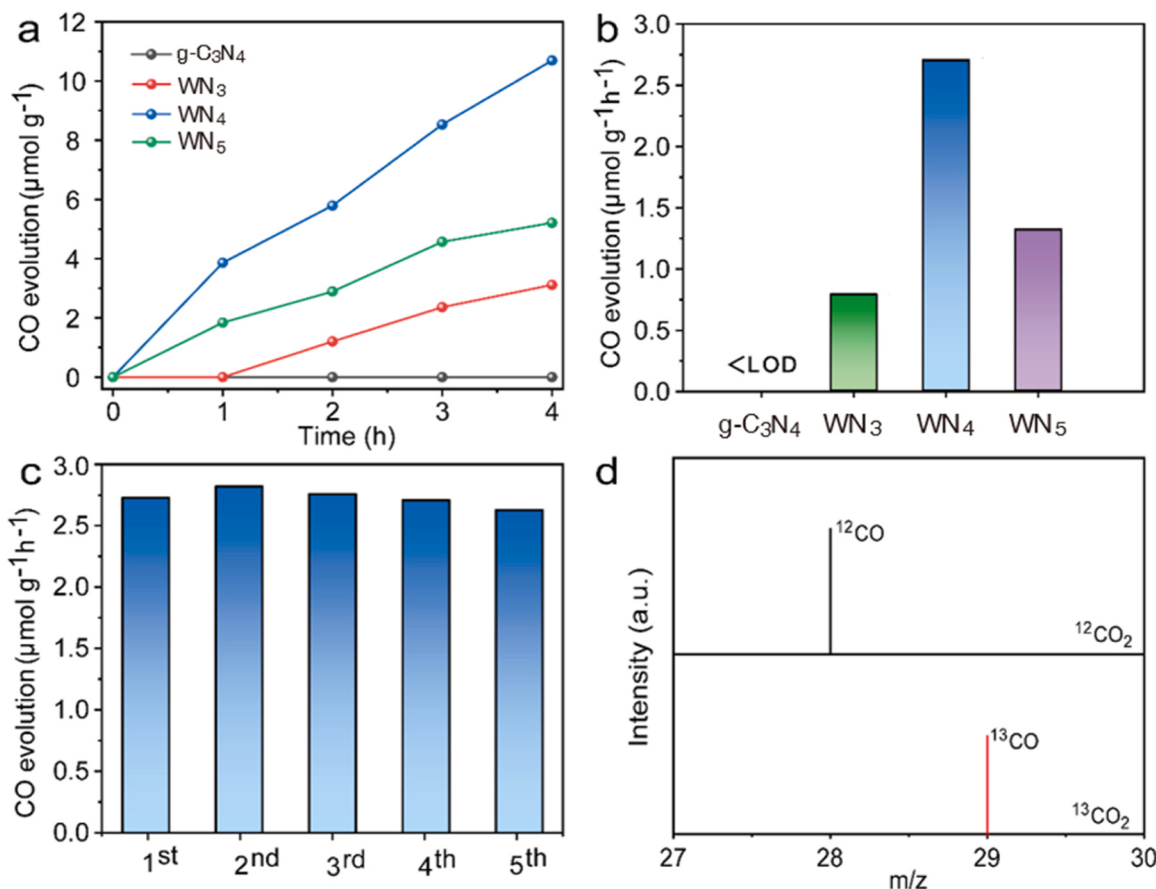


Fig. 4. (a) Profiles of CO evolution versus irradiation time and (b) the average CO evolution rate over 4-h irradiation, for the photocatalytic CO₂RR with g-C₃N₄, WN₃, WN₄ and WN₅. (c) Cycling tests for photocatalytic CO₂RR over WN₄ sample. (d) GC-MS analysis of products from photocatalytic CO₂RR over WN₄ sample, using isotope labelled ¹²CO₂ and ¹³CO₂ as the carbon sources, respectively.

Interestingly, significant difference in the CO evolution rate is achieved on WN_x samples with varied W-N coordination numbers, among which the WN₄ sample exhibits the most prominent CO yield of 2.67 μmol h⁻¹g⁻¹, being 3.4 time and 2.1 time larger than that observed with the WN₃ (0.78 μmol h⁻¹g⁻¹) and WN₅ (1.30 μmol h⁻¹g⁻¹) sample, respectively (Fig. 4b). These observations clearly indicate that the local coordination of single-atom W sites indeed plays a vital role in determining the photocatalytic CO₂RR, and a moderate coordination number is favorable for the CO generation. Notably, the WN_x samples also exhibit good stability during the photocatalytic CO₂RR. As reflected by the cyclic photocatalytic performances of the WN₄ sample, the CO yield rate remains almost unchanged during five consecutive photocatalytic cycles, which further collaborates the effective coordination between W atoms and the g-C₃N₄ lattice that would maintain the local chemical environment of single-atom W during the photocatalytic reactions (Fig. 4c).

Since the carbonaceous substrate g-C₃N₄ is involved in our photocatalysts, it is necessary to track for the origin of carbon elements in the CO product. We utilize the ¹³C isotope labeled CO₂ as reactant to ascertain the photoreaction products, which can be detected by gas chromatography-mass spectrometry (GC-MS). As shown in Fig. 4d, only one peak of ¹³CO (m/z=29) is detected when ¹³CO₂ is used as the reactant, which is distinct from the peak of ¹²CO (m/z=28) that originated from the carbon source of ¹²CO₂. It clearly indicates that the photocatalytic CO product we observed is generated from CO₂ reduction, rather than those escape from the photocatalysts or other carbon impurities.

In situ diffuse reflectance infrared Fourier transform spectroscopy (DRIFTS) is then used to dynamically monitor the adsorbed surface

species and CO₂-derived intermediates during the photocatalytic reactions, for a close inspect on the photocatalytic mechanism determined by the coordination microenvironment of single-atom W sites. It can be seen that the pristine g-C₃N₄ as a reference sample depicts nearly unchanged background IR signals during visible irradiation for 2 h since the introduction of humid CO₂ (Fig. 5a), suggestive of a rather poor CO₂-adsorption ability on bare g-C₃N₄ surface [31]. When monitored under similar conditions, significant peaks attributable to the CO₂-derived intermediates can be observed on the three WN_x samples (WN₃, WN₄ and WN₅), which emerge at almost identical wavenumbers but with different intensities (Fig. 5b, c, d). Such a phenomenon suggests similar transformation pathway but distinct activities for photocatalytic CO₂RR on the three WN_x samples [32]. As indicated by the peak located at 1568 cm⁻¹, attributable to the key intermediate of COOH* radical emblematising CO₂ reduction [35], a monotonous increase in its intensity can be observed for the three WN_x samples during the 120-min irradiation, which is most prominent for the WN₄ sample with respect to its counterparts of WN₃ and WN₅ (Figure S6). Then, a close examination is conducted for the DRIFTS curves of CO₂ and the intermediates during its reduction, by taking WN₄ photocatalyst as a typical example (Fig. 5c). When measured under visible irradiation after the introduction of humid CO₂, spectral signals attributed to CO₂ and the intermediates are detected, with the typical peaks located at 1418, 1447, 1508, 1518, 1594, 1614, and 1636 cm⁻¹ to CO₃²⁻ [33–35], and those located at 1431, 1474, 1484, 1497, 1652, and 1715 cm⁻¹ to HCO₃⁻ [33,36,37,40]. The presence of CO₃²⁻ and HCO₃⁻ intermediates suggest the dissolution of CO₂ in water after the introduction of humid CO₂. Upon prolonged irradiation, new absorption peaks appeared in the DRIFTS spectra, with the peaks at 1577, 1673, 1688 and 1742 cm⁻¹ belonging to HCOO⁻ [33,38,

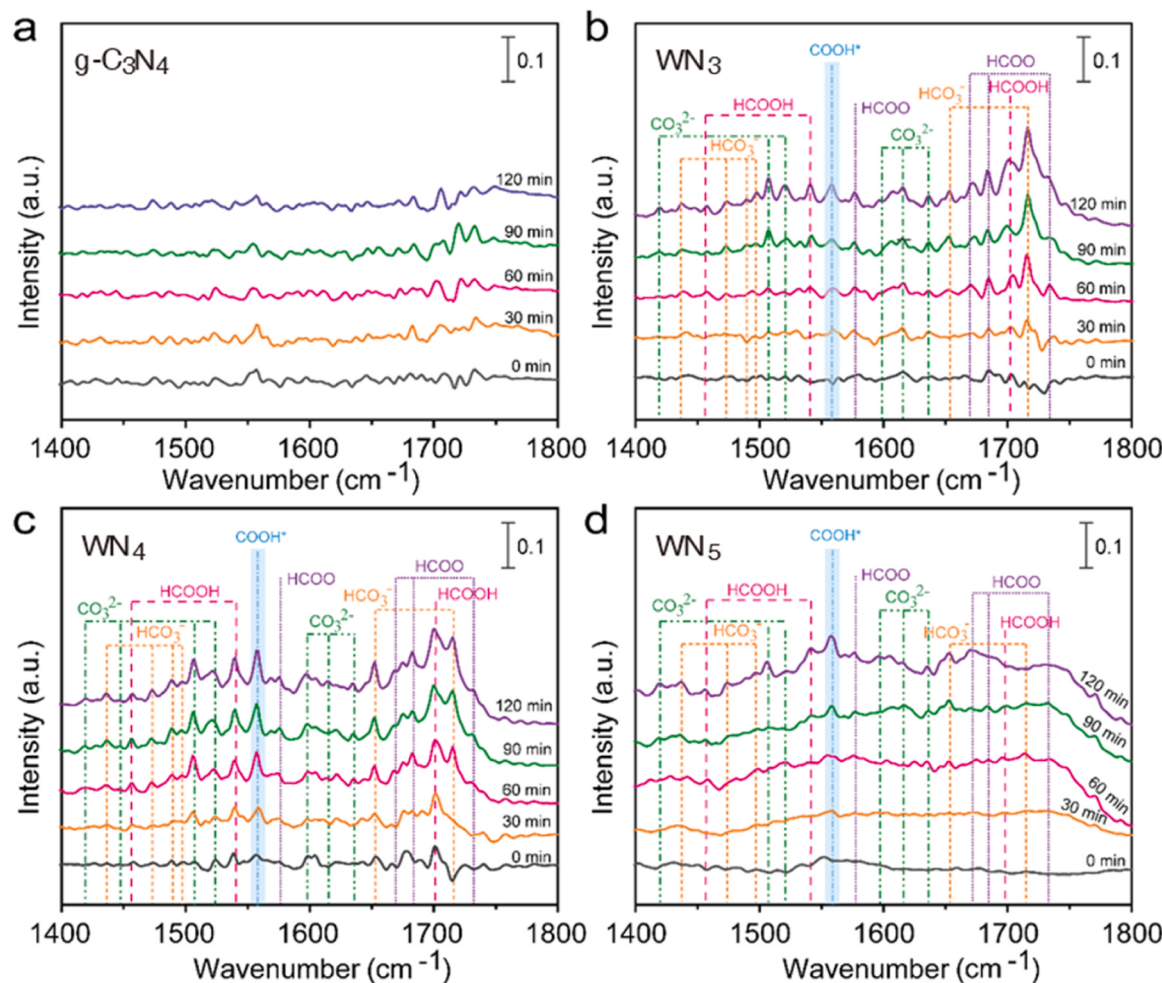
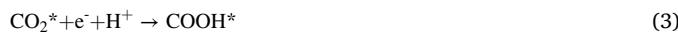


Fig. 5. The *in situ* DRIFT spectra recorded at 0, 30, 60, 90, and 120 min under visible light irradiation since the introduction of flowing CO_2 gas and H_2O vapor, with the photocatalyst of (a) $\text{g-C}_3\text{N}_4$, (b) WN_3 , (c) WN_4 , and (d) WN_5 , respectively.

[39] the peaks at 1457, 1542 and 1704 cm^{-1} to HCOOH [33,41], and 1568 cm^{-1} to COOH^* radicals [35]. The observed species such as HCOO , HCOOH and COOH^* are characteristic intermediates associated with the generation of CO during photocatalytic CO_2RR , verifying the high selectivity toward CO production with the WN_x samples. Based on the intermediate analysis, we can infer the photocatalytic CO_2RR mediated by our WN_x samples, with the reaction processes depicted by Eqs. 1–5 (the symbol * represents the species adsorbed on the photocatalyst surface). First, CO_2 molecules are adsorbed on the WN_x surface to be activated (Eq.1), accompanied by dissolution of H_2O into H^+ and OH^- (Eq.2). One pair of photogenerated electron and proton are added to the activated CO_2^* for the generation of COOH^* species (Eq.3), which is then reduced to adsorbed CO^* by receiving another pair of photogenerated electron and proton (Eq.4). At last, CO as the final product is released from the surface of WN_x (Eq.5).



2.4. Mechanism relevant to coordination microenvironment of WN_x samples

There are several contributing factors to the observed photocatalytic activities for CO_2RR , such as efficient light absorption, fast charge transfer and lowered activation energy for surface reactions, which may be altered along with the modifiable local coordination environment for the series of WN_x samples [42,43]. The light-harvesting ability of as-prepared samples can be directly revealed by UV-vis diffuse absorption spectra (Fig. 6a), where only slightly altered light-harvesting in the UV-visible region can be differentiated among pristine $\text{g-C}_3\text{N}_4$ and the three WN_x samples. According to the Tauc plot extracted from the UV-visible absorption spectra, bandgap can be obtained for the samples, with the value determined to be 2.93 eV for pristine $\text{g-C}_3\text{N}_4$ and 2.88, 2.82, 2.85 for WN_3 , WN_4 , WN_5 , respectively (inset of Fig. 6a). Accordingly, the anchoring of single-atom W would cause a slight decrease in bandgap with respect to the pristine $\text{g-C}_3\text{N}_4$, which may contribute to the overall photocatalytic performances by an increased utilization of incident photons especially in the visible region. However, it definitely cannot be the exclusive explanation for the drastic difference in performance shown by WN_x samples, which are designed with nearly identical chemical constitution but varied coordination environments at single-atom W sites. The steady state photoluminescence (PL) spectroscopy is then employed to disclose the separation efficiency of the photogenerated charges carriers (Fig. 6b). All the examined samples exhibit prominent PL emission peak at 450 nm (excited with 325 nm),

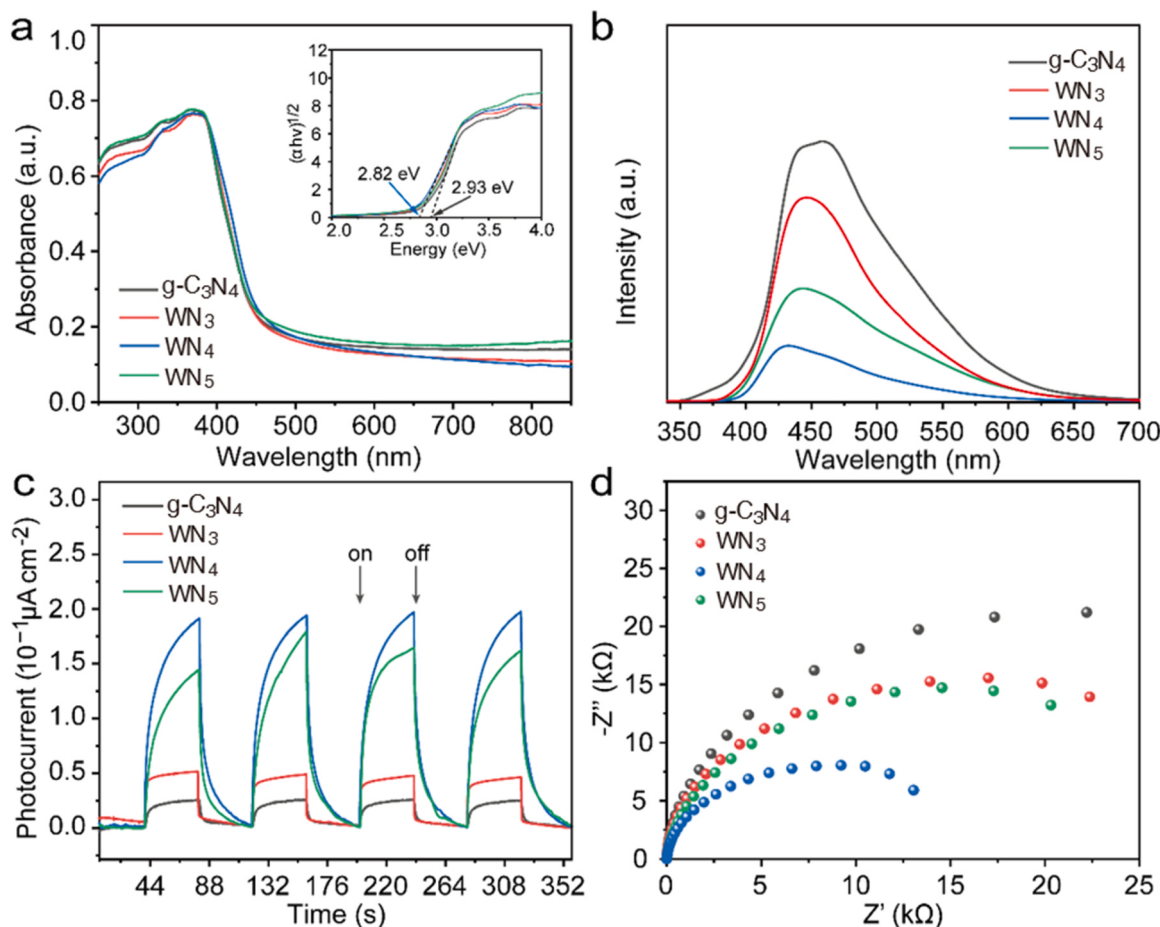


Fig. 6. (a) UV-visible absorption spectra of samples with the corresponding Tauc plot shown in inset, (b) PL spectra, (c) transient photocurrent (TPR) test and (d) electrochemical impedance curves (EIS) for g-C₃N₄, WN₃, WN₄, and WN₅ samples.

attributable to the recombination of the photogenerated electron-hole pairs in the g-C₃N₄ framework. Notably, the WN₄ sample depicts the smallest PL emission peak, followed by WN₅, WN₃ and the pristine g-C₃N₄ sample, which is in the same descending trend with the photocatalytic CO₂RR activity as reflected by the CO generation rate. Since a relatively small emission peak in PL spectra usually indicates a suppressed recombination in the photogenerated charge carriers and consequently enhanced photocatalytic activity [44], improved charge carrier separation realized by fine-tuning coordination at the sites of W may be contributable to the photocatalytic efficiency of WN_x samples.

The transient photocurrent (TPR) test is then employed to provide information about the charge carrier transport within the photocatalytic materials. As depicted in Fig. 6c, the largest photocurrent is observed with the WN₄ sample, followed by WN₅, WN₃ and pristine g-C₃N₄. Clearly, the anchoring of single-atom W would facilitate charge carrier transport in g-C₃N₄ framework as a function of coordination numbers, which is rather desirable for the g-C₃N₄ materials. Such a trend is further confirmed by the electrochemical impedance curves (EIS) shown in Fig. 6d, where WN₄ has the smallest radius of the EIS curve with respect to its counterparts with 3 or 5 coordination numbers, implying fluent carrier transport can also be achieved if the SACs take a proper coordination microenvironment. Further, we check the chemisorption of CO₂ onto the surface of photocatalyst by resorting to TG analysis (Figure S7), since it is the initial step ahead of the charge carrier transfer and its final conversion. The change in sample mass before and after aeration is tested by passing CO₂ gas at 50 °C, which exhibits an increase in CO₂ adsorption from a relatively small value of 460 $\mu\text{mol g}^{-1}$ for pristine g-C₃N₄ to 837.0, 1307.7, 1715.0 $\mu\text{mol g}^{-1}$ for WN₃, WN₅, WN₄, respectively, again related to the number of W-N coordination.

From the results above, we can infer that the enhanced adsorption of CO₂, efficient separation of photogenerated charge carriers, and the fluent migration of photogenerated electrons to CO₂ molecules contribute together to the enhanced photocatalytic CO₂RR, which can be simultaneously optimized through a large-span manipulation in the coordination numbers for the W SACs.

2.5. DFT calculations

For a further illustration about the interaction between CO₂ and WN_x determined by local coordination microenvironment, theoretical simulations are conducted based on calculations on differential charge density, Bader charge analysis, projected density of states (PDOS) and free energy for reaction path (CO₂ to CO). As shown by the charge density distribution diagram in Fig. 7a, three relatively stable coordination structures, namely, WN₃, WN₄ and WN₅, can be formed between W atom and the g-C₃N₄ lattice, exhibiting different electron cloud distribution around the single-atom W sites where CO₂ molecules are anchored. Then, with the adsorption of CO₂ molecule, 0.03, 0.52 and 0.09 electron can be transferred to one CO₂ molecule from WN₃, WN₄ and WN₅, respectively. The results clearly indicate an efficient activation of CO₂ molecule by WN₄ when compared to its counterparts with other coordination number of 3 and 5. Fig. 7b-d compare the PDOS of WN₃, WN₄ and WN₅ after CO₂ adsorption, where the three samples exhibit density of states across the Fermi level, as an indication of improved electrical conductivity that would facilitate charge carrier mobilization. In significant contrast, bare g-C₃N₄ exhibit negligible density of states over the Fermi level concerning about CO₂ adsorption [28]. Further, the overlapped profiles in PDOS of WN₃, WN₄ and WN₅ with CO₂ adsorption

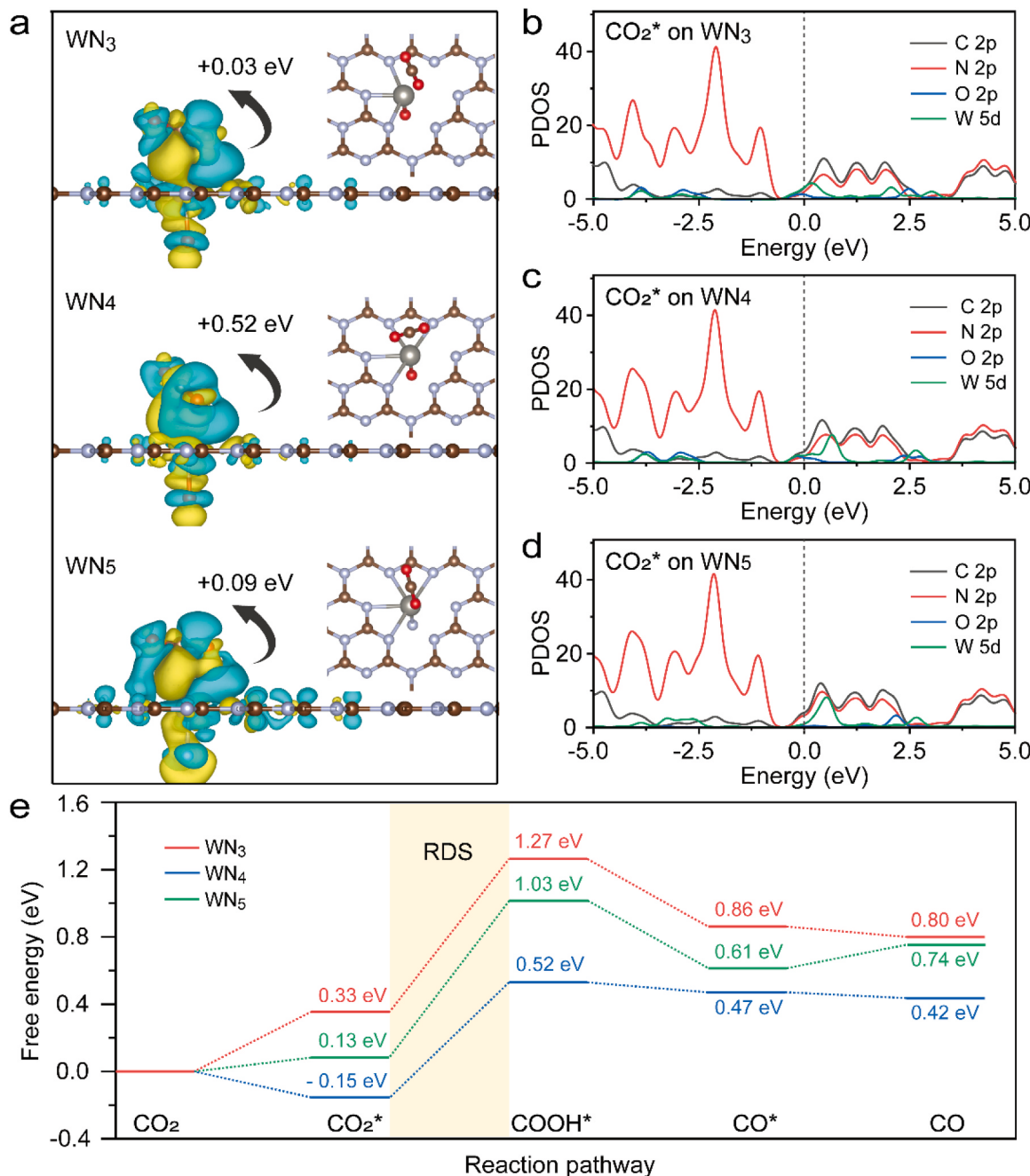


Fig. 7. (a) The charge density differences and Bader charge transfer for CO_2 adsorbed on WN_3 , WN_4 and WN_5 (The inset shows three models of single-atom W modified $\text{g-C}_3\text{N}_4$). The enlarged projected density of states (PDOS) for CO_2^* adsorbed on (b) WN_3 , (c) WN_4 and (d) WN_5 , respectively. (e) Calculated free energy diagrams for the transformation from CO_2 to CO through the photocatalytic CO_2RR on WN_3 , WN_4 and WN_5 .

suggest a hybridization between W 5d and the 2p orbitals from C, N and O, indicating that single-atom W anchored by the $\text{g-C}_3\text{N}_4$ lattice would act as binding center for CO_2 molecule adsorption to initiate the subsequent photocatalytic reactions. At last, free energies for the reaction pathway (CO_2 to CO) on different WN_x samples are surveyed in Fig. 7e, which reflect a four-step pathway initiated from CO_2 adsorption and ended by CO product.

3. Conclusion

Tailored coordination microenvironment of single-atom W is realized by W metal incorporated $\text{g-C}_3\text{N}_4$ samples as SACs, accompanied by a post annealing treatment under NH_3 atmosphere. It is found that the

coordination microenvironment of central W plays a vital role in determining the CO generation as the main product of photocatalytic CO_2RR , where the WN_4 sample with a moderate coordination number of 4 shows the highest photocatalytic activity, exhibiting the most prominent CO yield of $2.67 \mu\text{mol h}^{-1}\text{g}^{-1}$, several times larger exceeding the SACs with other coordination numbers (such as 3 and 5). This phenomenon is disclosed to be related with enhanced CO_2 chemisorption and efficient charge-carrier separation/transport, realized simultaneously by an optimized W-N coordination number. The results confirm that rational manipulation for coordination microenvironment of single atoms would be an effective means to improve their photocatalytic activities, drastic, which would pave the way for SACs in photocatalytic applications.

CRediT authorship contribution statement

Shan Cong: Writing – review & editing, Writing – original draft, Supervision, Methodology, Funding acquisition, Formal analysis, Conceptualization. **Zhigang Zhao:** Validation, Supervision, Funding acquisition. **Juan Wang:** Software, Validation, Formal analysis. **Kangle Lv:** Methodology, Validation, Resources, Supervision. **Jinyu Zhou:** Writing – review & editing, Writing – original draft, Validation, Methodology, Investigation, Formal analysis, Data curation, Visualization. **Xiuling Zha:** Writing – review & editing, Writing – original draft, Investigation, Formal analysis, Data curation, Visualization. **Zhigang Chen:** Software, Investigation, Data curation. **Kaining Li:** Methodology, Investigation, Data curation, Formal analysis. **Hongzhao Sun:** Data curation, Formal analysis.

Declaration of Competing Interest

The authors declare no conflict of interest.

Data availability

Data will be made available on request.

Acknowledgements

This work is supported by the National Natural Science Foundation of China (22175198 and 52172299). S. C would like to acknowledge the support from the External Cooperation Program of the Chinese Academy of Sciences (320GJHZ20230111MI), Suzhou Industrial Science and Technology Program (SYC2022036), and High-end Talents Program of Jiangxi Province (jxsq2023101113). The authors are grateful for the technical support for Nano-X from Suzhou Institute of Nano-Tech and Nano-Bionics, Chinese Academy of Sciences (SINANO).

Appendix A. Supporting information

Supplementary data associated with this article can be found in the online version at [doi:10.1016/j.apcatb.2024.123911](https://doi.org/10.1016/j.apcatb.2024.123911).

References

- [1] D. Broadstock, Q. Ji, S. Managi, D. Zhang, *Resour. Conserv. Recycl.* 169 (2021) 105472.
- [2] W. Liu, P. Fu, Y. Zhang, H. Xu, H. Wang, M. Xing, *Proc. Natl. Acad. Sci. USA* 120 (2023) e2218813120.
- [3] M. Ran, H. Xu, Y. Bao, Y. Zhang, J. Zhang, M. Xing, *Angew. Chem. Int. Ed.* 62 (2023) e202303728.
- [4] J. Fu, K. Jiang, X. Qiu, J. Yu, M. Liu, *Mater. Today* 32 (2020) 222–243.
- [5] K. Li, B. Peng, T. Peng, *ACS Catal.* 6 (2016) 7485–7527.
- [6] T. Wang, Q. Zhao, Y. Fu, C. Lei, B. Yang, Z. Li, L. Lei, G. Wu, Y. Hou, *Small Methods* 3 (2019) 1900210.
- [7] L. Zeng, C. Xue, *Nano Res.* 14 (2020) 934–944.
- [8] C. f Li, W. g Pan, Z. r Zhang, T. Wu, R. t Guo, *Small* 19 (2023) 2300460.
- [9] Q. Wang, D. Zhang, Y. Chen, W.-F. Fu, X.-J. Lv, *ACS Sustain. Chem. Eng.* 7 (2019) 6430–6443.
- [10] Q. Zhao, W. Yao, C. Huang, Q. Wu, Q. Xu, *ACS Appl. Mater. Interfaces* 9 (2017) 42734–42741.
- [11] T. Sun, Y. Li, T. Cui, L. Xu, Y.-G. Wang, W. Chen, P. Zhang, T. Zheng, X. Fu, S. Zhang, Z. Zhang, D. Wang, Y. Li, *Nano Lett.* 20 (2020) 6206–6214.
- [12] R. Shen, L. Hao, Y.H. Ng, P. Zhang, A. Arramel, Y. Li, X. Li, *Chin. J. Catal.* 43 (2022) 2453–2483.
- [13] X.Y. Dong, Y.N. Si, Q.Y. Wang, S. Wang, S.Q. Zang, *Adv. Mater.* 33 (2021) 2101568.
- [14] Y. Feng, C. Wang, P. Cui, C. Li, B. Zhang, L. Gan, S. Zhang, X. Zhang, X. Zhou, Z. Sun, K. Wang, Y. Duan, H. Li, K. Zhou, H. Huang, A. Li, C. Zhuang, L. Wang, Z. Zhang, X. Han, *Adv. Mater.* 34 (2022) 2109074.
- [15] T. He, C. Zhang, L. Zhang, A. Du, *Nano Res.* 12 (2019) 1817–1823.
- [16] O.Y. Bisen, A.K. Yadav, K.K. Nanda, *ACS Appl. Mater. Interfaces* 12 (2020) 43586–43595.
- [17] W.-J. Ong, L.-L. Tan, Y.H. Ng, S.-T. Yong, S.-P. Chai, *Chem. Rev.* 116 (2016) 7159–7329.
- [18] Y. Li, F. Gong, Q. Zhou, X. Feng, J. Fan, Q. Xiang, *Appl. Catal. B* 268 (2020) 118381.
- [19] J. Luo, J. Wang, G. Li, Q. Huo, Y. Liu, *Chem. Commun.* 49 (2013) 11433–114351.
- [20] C. Zhou, C. Lai, D. Huang, G. Zeng, C. Zhang, M. Cheng, L. Hu, J. Wan, W. Xiong, M. Wen, X. Wen, L. Qin, *Appl. Catal. B* 220 (2018) 202–210.
- [21] Y. Li, D. Zhang, X. Feng, Q. Xiang, *Chin. J. Catal.* 41 (2020) 21–30.
- [22] J. Jiang, L. Ou-yang, L. Zhu, A. Zheng, J. Zou, X. Yi, H. Tang, *Carbon* 80 (2014) 213–221.
- [23] X. Zhang, X. Xie, H. Wang, J. Zhang, B. Pan, Y. Xie, *J. Am. Chem. Soc.* 135 (2012) 18–21.
- [24] J. Xu, L. Zhang, R. Shi, Y. Zhu, *J. Mater. Chem. A* 1 (2013) 14766–14772.
- [25] Z. Chen, W. Gong, Z. Liu, S. Cong, Z. Zheng, Z. Wang, W. Zhang, J. Ma, H. Yu, G. Li, W. Lu, W. Ren, Z. Zhao, *Nano Energy* 60 (2019) 394–403.
- [26] G. Zhang, S. Zang, X. Wang, *ACS Catal.* 5 (2015) 941–947.
- [27] S. Roy, E. Reisner, *Angew. Chem. Int. Ed.* 58 (2019) 12180–12184.
- [28] J. Fu, L. Zhu, K. Jiang, K. Liu, Z. Wang, X. Qiu, H. Li, J. Hu, H. Pan, Y.-R. Lu, T.-S. Chan, M. Liu, *Chem. Eng. J.* 415 (2021) 128982.
- [29] J.S. Lee, J.E. Yie, *Korean J. Chem. Eng.* 8 (1991) 164–167.
- [30] Y. Wang, X. Bai, H. Qin, F. Wang, Y. Li, X. Li, S. Kang, Y. Zuo, L. Cui, *ACS Appl. Mater. Interfaces* 8 (2016) 17212–17219.
- [31] C. Yang, Q. Tan, Q. Li, J. Zhou, J. Fan, B. Li, J. Sun, K. Lv, *Appl. Catal. B* 268 (2020) 118738.
- [32] W. Wang, Z. Qu, L. Song, Q. Fu, *J. Energy Chem.* 47 (2020) 18–28.
- [33] X. Jiao, X. Li, X. Jin, Y. Sun, J. Xu, L. Liang, H. Ju, J. Zhu, Y. Pan, W. Yan, Y. Lin, Y. Xie, *J. Am. Chem. Soc.* 139 (2017) 18044–18051.
- [34] C. Han, R. Zhang, Y. Ye, L. Wang, Z. Ma, F. Su, H. Xie, Y. Zhou, P.K. Wong, L. Ye, *J. Mater. Chem. A* 7 (2019) 9726–9735.
- [35] J. Di, C. Chen, S.-Z. Yang, S. Chen, M. Duan, J. Xiong, C. Zhu, R. Long, W. Hao, Z. Chi, H. Chen, Y.-X. Weng, J. Xia, L. Song, S. Li, H. Li, Z. Liu, *Nat. Commun.* 10 (2019) 2840.
- [36] K. Liu, X. Li, L. Liang, J. Wu, X. Jiao, J. Xu, Y. Sun, Y. Xie, *Nano Res.* 11 (2018) 2897–2908.
- [37] A. Meng, S. Wu, B. Cheng, J. Yu, J. Xu, *J. Mater. Chem. A* 6 (2018) 4729–4736.
- [38] Y. Huo, J. Zhang, K. Dai, Q. Li, J. Lv, G. Zhu, C. Liang, *Appl. Catal. B* 241 (2019) 528–538.
- [39] F. Xu, J. Zhang, B. Zhu, J. Yu, J. Xu, *Appl. Catal. B* 230 (2018) 194–202.
- [40] J. Fu, B. Zhu, C. Jiang, B. Cheng, W. You, J. Yu, *Small* 13 (2017) 1603938.
- [41] P. Xia, B. Zhu, J. Yu, S. Cao, M. Jaroniec, *J. Mater. Chem. A* 5 (2017) 3230–3238.
- [42] C. Yao, R. Wang, Z. Wang, H. Lei, X. Dong, C. He, *J. Mater. Chem. A* 7 (2019) 27547–27559.
- [43] A. Yuan, H. Lei, Z. Wang, X. Dong, *J. Colloid Interface Sci.* 560 (2020) 40–49.
- [44] Y. Xia, Z. Tian, T. Heil, A. Meng, B. Cheng, S. Cao, J. Yu, M. Antonietti, *Joule* 3 (2019) 2792–2805.